IJMMM International Journal of Minerals, Metallurgy and Materials 矿物冶金与材料学报（英文版）

Metal–organic decomposition growth of thin film metastable perovskite nickelates with kinetically improved quantum transitions

Haiyan Li, Yuzhao Wang, Fanqi Meng, Wei Mao, Xingzhong Cao, Yi Bian, Hao Zhang, Yong Jiang, Nuofu Chen, and Jikun Chen

Cite this article as:
Haiyan Li, Yuzhao Wang, Fanqi Meng, Wei Mao, Xingzhong Cao, Yi Bian, Hao Zhang, Yong Jiang, Nuofu Chen, and Jikun Chen, Metal–organic decomposition growth of thin film metastable perovskite nickelates with kinetically improved quantum transitions, *Int. J. Miner. Metall. Mater.*, 30(2023), No. 12, pp. 2441-2450. https://doi.org/10.1007/s12613-023-2703-9

View the article online at SpringerLink or IJMMM Webpage.

Articles you may be interested in

Ying-zhi Chen, Dong-jian Jiang, Zheng-qi Gong, Jing-yuan Li, and Lu-ning Wang, Anodized metal oxide nanostructures for photoelectrochemical water splitting, *Int. J. Miner. Metall. Mater.*, 27(2020), No. 5, pp. 584-601. https://doi.org/10.1007/s12613-020-1983-6

Tao Wei, Zao-hong Zhang, Qi Zhang, Jia-hao Lu, Qi-ming Xiong, Feng-yue Wang, Xin-ping Zhou, Wen-jia Zhao, and Xiang-yun Qiu, Anion-immobilized solid composite electrolytes based on metal-organic frameworks and superacid ZrO_2 fillers for high-performance all solid-state lithium metal batteries, *Int. J. Miner. Metall. Mater.*, 28(2021), No. 10, pp. 1636-1646. https://doi.org/10.1007/s12613-021-2289-z

Qiang Ge, Wen-hui Kong, Xin-qian Liu, Ying-min Wang, Li-feng Wang, Ning Ma, and Yan Li, Hydroxylated graphene quantum dots as fluorescent probes for sensitive detection of metal ions, *Int. J. Miner. Metall. Mater.*, 27(2020), No. 1, pp. 91-99. https://doi.org/10.1007/s12613-019-1908-4

Jing-qun Yin, Zhi-qiang Zou, and Jun Tian, Preparation of crystalline rare earth carbonates with large particle size from the lixivium of weathered crust elution-deposited rare earth ores, *Int. J. Miner. Metall. Mater.*, 27(2020), No. 11, pp. 1482-1488. https://doi.org/10.1007/s12613-020-2066-4

Xiao-li Xi, Ming Feng, Li-wen Zhang, and Zuo-ren Nie, Applications of molten salt and progress of molten salt electrolysis in secondary metal resource recovery, *Int. J. Miner. Metall. Mater.*, 27(2020), No. 12, pp. 1599-1617. https://doi.org/10.1007/s12613-020-2175-0

Xiao-hui Ning, Chen-zheng Liao, and Guo-qing Li, Electrochemical properties of Ca–Pb electrode for calcium-based liquid metal batteries, *Int. J. Miner. Metall. Mater.*, 27(2020), No. 12, pp. 1723-1729. https://doi.org/10.1007/s12613-020-2150-9

IJMMM WeChat

QQ author group

International Journal of Minerals, Metallurgy and Materials
Volume 30, Number 12, December 2023, Page 2441
https://doi.org/10.1007/s12613-023-2703-9

Metal–organic decomposition growth of thin film metastable perovskite nickelates with kinetically improved quantum transitions

Haiyan Li[1),*], *Yuzhao Wang*[2),*], *Fanqi Meng*[3),*], *Wei Mao*[4),*], *Xingzhong Cao*[5)], *Yi Bian*[1)], *Hao Zhang*[2)], *Yong Jiang*[1)], *Nuofu Chen*[2)], *and Jikun Chen*[1),✉]

1) Beijing Advanced Innovation Center for Materials Genome Engineering, School of Materials Science and Engineering, University of Science and Technology Beijing, Beijing 100083, China
2) School of Renewable Energy, North China Electric Power University, Beijing 102206, China
3) School of Materials Science and Engineering, Peking University, Beijing 100871, China
4) School of Engineering, The University of Tokyo, 2-11-16 Yayoi, Bunkyo-ku, Tokyo 113-0032, Japan
5) Institute of High Energy Physics, Chinese Academy of Sciences, Beijing 100049, China
(Received: 7 April 2023; revised: 19 June 2023; accepted: 5 July 2023)

Abstract: The multiple quantum transitions within d-band correlation oxides such as rare-earth nickelates ($RENiO_3$) triggered by critical temperatures and/or hydrogenation opened up a new paradigm for correlated electronics applications, e.g. ocean electric field sensor, bio-sensor, and neuron synapse logical devices. Nevertheless, these applications are obstructed by the present ineffectiveness in the thin film growth of the metastable $RENiO_3$ with flexibly adjustable rare-earth compositions and electronic structures. Herein, we demonstrate a metal-organic decompositions (MOD) approach that can effectively grow metastable $RENiO_3$ covering a large variety of the rare-earth composition without introducing any vacuum process. Unlike the previous chemical growths for $RENiO_3$ relying on strict interfacial coherency that limit the film thickness, the MOD growth using reactive isooctanoate percussors is tolerant to lattice defects and therefore achieves comparable film thickness to vacuum depositions. Further indicated by positron annihilation spectroscopy, the $RENiO_3$ grown by MOD exhibit large amount of lattice defects that improves their hydrogen incorporation amount and electron transfers, as demonstrated by the resonant nuclear reaction analysis and near edge X-ray absorption fine structure analysis. This effectively enlarges the magnitude in the resistance regulations in particular for $RENiO_3$ with lighter RE, shedding a light on the extrinsic regulation of the hydrogen induced quantum transitions for correlated oxides semiconductors kinetically via defect engineering.

Keywords: metal-insulator transition; rare earth nickelates; lattice defects; hydrogen incorporation; metal-organic decomposition

1. Introduction

The ionic switchable quantum transitions within d-band correlated transitional oxides open up a new paradigm to establish new electronic material phases and explore their potential new applications in correlated electronic devices [1–13]. As one such representative family of quantum materials, the perovskite structured rare-earth nickelates ($RENiO_3$) exhibit exceptional complex electronic and magnetic phase diagram and reversible multiple ground state quantum transitions [1–6,14–19]. Typically, the Ni^{3+} charge disproportionation (or anti-disproportionation) between $t_{2g}^6e_g^1$ and $t_{2g}^6e_g^{1\pm\delta}$ orbital configurations at critical temperature (T_{MIT}) enables metal to insulator transition (MIT) of $RENiO_3$ [14–15]. An overwhelming advantage of $RENiO_3$ beyond other MIT materials is their continuously adjustable T_{MIT} over a wide temperature range of 100–600 K by simply regulating the rare-earth composition [14]. The rare-earth radius adjusts the distortion of the NiO_6 octahedral that determines the relative stability of the insulating and metallic phases, and thereby the T_{MIT}. In 2014, a reversible electronic transition of $RENiO_3$ as triggered by chemical and/or electrochemical electron doping via hydrogen (proton) was demonstrated, in which case the orbital configuration transits towards an electron highly localized state of $t_{2g}^6e_g^2$ while maintaining high proton conductance [4]. The discovery of the hydrogen induced quantum transition further enriches correlated electronic applications of $RENiO_3$ in ocean electric field sensor [1], correlated fuel cell [2], neuron synapse logical devices [5–6], bio-sensor [7], etc. Furthermore, another new electronic state associated to $t_{2g}^6e_g^3$ orbital configuration was discovered for nickelates in 2019 in heavily hydrogenated $Nd_{0.8}Sr_{0.2}NiO_3/SrTiO_3$ heterostructure [20] or proton aggregated grain boundaries of $SmNiO_3$ (SNO) [21]. These discoveries shed a light to explore more exciting quantum phenomenon such as the nickelates-based superconductivity and multiple electronic

*These authors contributed equally to this work.
✉ Corresponding author: Jikun Chen E-mail: jikunchen@ustb.edu.cn
© University of Science and Technology Beijing 2023

transitions within the material family relevant to rare-earth nickelates [20–24].

Nevertheless, a central obstacle to overcome for both above fundamental explorations and electronic applications of $RENiO_3$ is associated to their intrinsic material metastability [14]. Unlike conventional oxides, the $RENiO_3$ exhibits a positive formation free energy (ΔG) that hinders their synthesis via conventional solid state reactions, in particular, for $RENiO_3$ with heavy rare-earth elements [15,25]. In general, the vacuum deposition approaches, e.g. pulsed laser deposition (PLD), sputtering or metal organic chemical vapor deposition, can be used to only grow $RENiO_3$ thin films with light or middle rare-earth compositions (e.g. $NdNiO_3$ (NNO), $PrNiO_3$, and $SmNiO_3$) that shows MIT properties [25–30]. Although we previously achieved the ultrathin film growth of $EuNiO_3$ and $GdNiO_3$ on single crystal $LaAlO_3$ (LAO) by developing a high pressure assisted chemical approaches based on $RE(NiO_3)_3$ and $Ni(AC)_2$ precursors, the deposition thickness cannot be further increased to beyond ~20 nm [15]. This reveals the high reliance in their heterogenous growth to the interfacial coherency with the lattice template of the single crystalline perovskite substrates that is necessary in reducing the positive ΔG of $RENiO_3$. It limits the deposition thickness since the presence of lattice defects or misfits will destroy the above heterogenous process and impedes the further heterogeneous growth of the metastable $RENiO_3$ as metastable perovskites. It is worth noticing that up to date, the thin film growth for the highly metastable $RENiO_3$ with middle or heavy rare-earth composition (e.g. RE heavier than Eu) at deposition thickness exceeding ~20 nm are rarely reported yet.

In this work, we developed a metal–organic decomposition (MOD) approach within high oxygen pressures that achieves the effective growth of $RENiO_3$ films covering a large variety of the rare-earth composition and a large deposition thickness comparable to their vacuum depositions. The high reactivity of the rare-earth isooctanoate precursors used in the MOD improves the formation of $RENiO_3$ as metastable perovskites and relieve their previous reliance to heterogenous growth following the lattice template of the substrates. This allows the growth of the heavy rare-earth $RENiO_3$ thin films with high defect density or in polycrystallinity as indicated by positron annihilation spectroscopy (PAS), while preserving their MIT properties. Further assisted by resonant nuclear reaction analysis (NRA), near edge X-ray absorption fine structure (NEXAFS) analysis, we demonstrated that the presence of lattice defects results in more pronounced variations in electronic structure of $RENiO_3$ upon hydrogenation. This highlights the overlooked role in extrinsic defect engineering that kinetically improves the regulations in electronic structures and transportations for the hydrogen related Mottronic transitions of $RENiO_3$.

2. Experimental

2.1. Synthesis of samples

Fig. 1(a) illustrates the high oxygen pressure assisted metal organic decomposition processes as used to grow the $RENiO_3$ films. In brief, the chemical precursors of $Ni(C_7H_{15}COO)_2$ and $RE(C_7H_{15}COO)_3$ were made by using $RE(AC)_3$ or $Ni(AC)_2$ to react with excess $C_7H_{15}COOH$ and $NH_3{\cdot}H_2O$, via the following two reactions:

$$RE(AC)_3 + 3C_7H_{15}COOH + 3NH_3H_2O \rightarrow RE(C_7H_{15}COO)_3 \downarrow + 3NH_4AC + 3H_2O \quad (1)$$

$$Ni(AC)_2 + 2C_7H_{15}COOH + 2NH_3H_2O \rightarrow Ni(C_7H_{15}COO)_2 \downarrow + 2NH_4AC + 2H_2O \quad (2)$$

After drying in air at 120°C, as made chemical precursors were mixed at equal stoichiometry and dissolved in xylene at a concentration of 0.1mol/L, and the solution was spin-coated on $LaAlO_3$ (001) substrate. The spin coated samples were annealed at 15 MPa high oxygen pressure at 450°C for 1 h for the decomposition of the metal organic precursors, and afterwards annealed at 850°C for 2 h to trigger their crystallization as $RENiO_3$.

2.2. Characterization

The cross-section morphologies of $RENiO_3/LaAlO_3$ (001) grown by MOD were characterized by the high-angle annular dark-field (HAADF) images. The temperature dependences of the resistivity (ρ–T) of the samples were measured by the Physical Property Measurement System (PPMS) as well as the constant temperature anemometer (CTA). The S-parameters of the samples were measured by the positron annihilation spectroscopy (PAS), derived from the shape of the Doppler broadening spectroscopy (DBS) of the annihilation generated γ-ray by $A/(A + B + C)$, where A, B, and C represent for the γ-ray collected in the wavelength range of 510.2–511.8, 505.1–508.4, and 513.6–516.9 keV, respectively. The resistances of $RENiO_3$ grown (with top platinum catalyst electrode) before and after annealing in 20vol% H_2 at 100°C for 30 min were measured by Keithley 4200. To further probe the variations in orbital configurations, the near edge X-ray absorption fine structure (NEXAFS) analysis was performed for the samples. The quantitative detection of the depth profile of hydrogen (^1H or $^1H^+$) within $RENiO_3$ was achieved by the resonant nuclear reaction analysis (NRA).

3. Results and discussion

3.1. $RENiO_3$ grown by MOD

Compared to the high pressure assisted spin coating approaches as reported previously, e.g. using $RE(C_7H_{15}COO)_3$ and $Ni(C_7H_{15}COO)_2$ as precursors [15], the isooctanoate based precursors exhibit long branched structure that cross-linked within the nonpolar solvent and have low decomposition temperature [31–32]. This results in more homogenous mixing of the RE and Ni containing processors and improves their reactivity. As further demonstrated in Figs. S1 and S2, the deposition intermediate products (e.g. annealing the chemical precursors in oxygen at 450°C) exhibit much smaller size for using the present MOD approach as compared to the one obtained in Ref. [11]. This provides the opportunity to relieve the previously high dependence in the nucleation of metastable $RENiO_3$ to the strict epitaxy relationship, and the

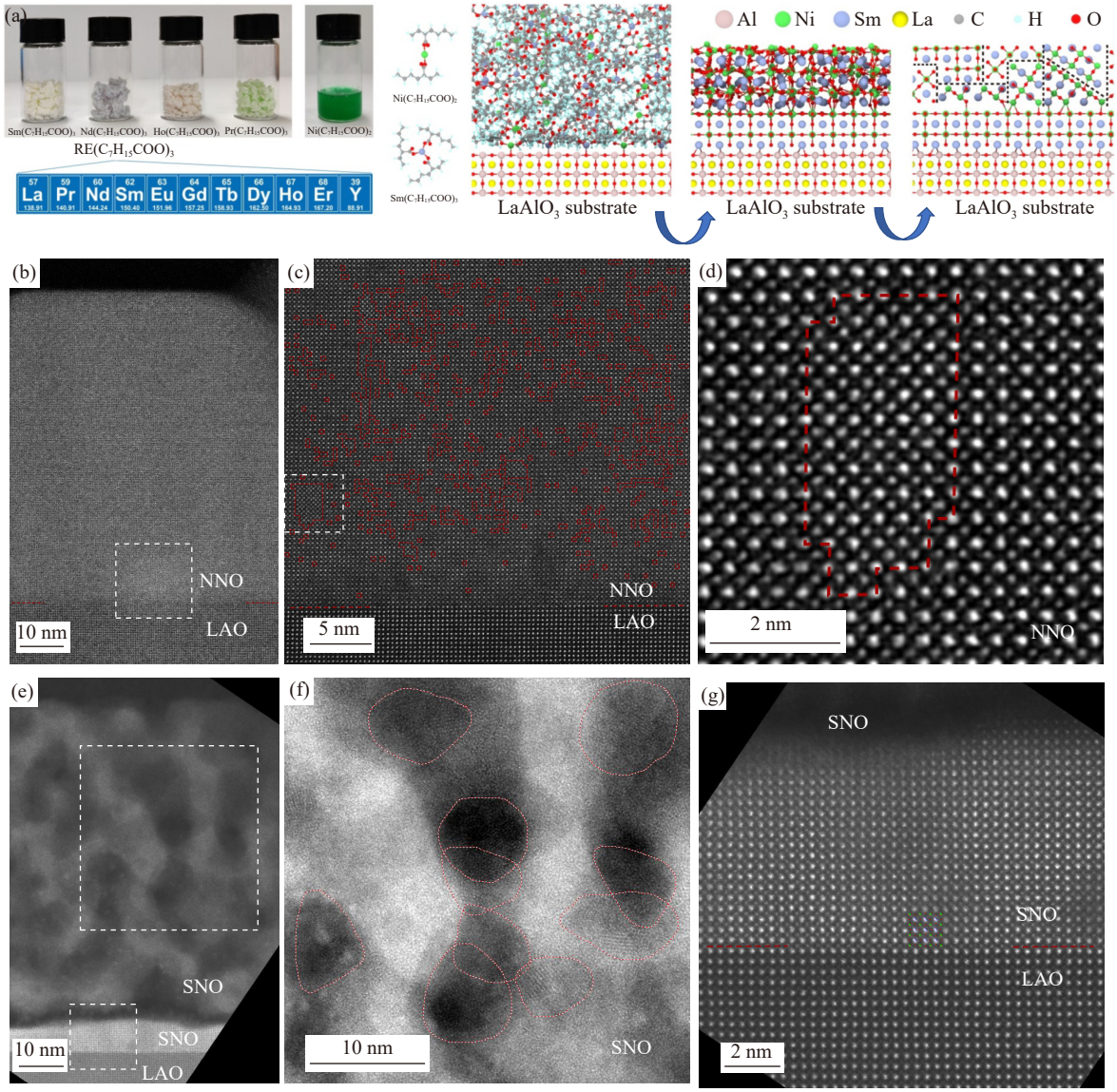

Fig. 1. (a) Schematic illustration of the high oxygen pressure assisted metal organic decomposition (MOD) approach. In brief, the isooctanoate based rare-earth and nickel metal-organic precursors (see photos in the left figures) were spin coated on $LaAlO_3$ (001) substrate. During the annealing process in high oxygen pressures, the precursors approaching to the surface of the substrate were decomposed and further coherently grown at quasi-single crystallinity. The precursors located away from the surface of the substrate were decomposed and further grown as polycrystalline $RENiO_3$. The high-angle annular dark-field (HAADF) images of the cross section morphology of (b–d) $NdNiO_3/LaAlO_3$ (001) and (e–g) $SmNiO_3/LaAlO_3$ (001) grown by MOD. The HAADF images shown for (c) and (d) are the amplified region to the squared region in (b) and (c), respectively. The anti-site defects between Nd and Ni within as-grown $NdNiO_3$ are marked in red in (c). The HAADF images shown for (f) and (g) are the amplified region to the upper and lower squared region in (e), respectively.

film can be grown thicker in even polycrystallinity. In addition, it is also worth noticing that the $C_7H_{15}COOH$ exhibits low cost among the $C_nH_{2n+1}COOH$. Compared to the more commonly used vacuum deposition approaches for $RENiO_3$, such as pulsed laser deposition or magnetic sputtering [25–30], the MOD approach can achieve a more flexible adjustment in the rare-earth composition by simply regulating the composition of the $RE(C_7H_{15}COO)_3$ precursor.

Herein, the MOD approach was used to successfully synthesize $RENiO_3$ films with rare-earth composition covering Nd, Sm, Eu, Gd, Tb, Dy, Ho, and Er, and also their mixture. Fig. 1(b–g) and Fig. S3 show the cross-section morphology for three representative $RENiO_3/LaAlO_3$ (001) samples grown by MOD, including $NdNiO_3$ (with low metastability), $SmNiO_3$ (with medium metastability), and $DyNiO_3$ (with high metastability). It can be seen that as-grown thin films of $NdNiO_3$ remain a similar crystal orientation compared to the $LaAlO_3$ substrate (see Fig. 1(b–d)), despite the presence of abundant lattice defects such as anti-site defect between Nd and Ni as marked in Fig. 1(c). This is in contrast to the situation for as grown $RENiO_3$ with heavier rare-earth compositions, such as $SmNiO_3/LaAlO_3$ (see Fig. 1(e–g) and $DyNiO_3/LaAlO_3$ (see Fig. S3). Their entire film thicknesses are of ~80 nm, which is similar to the situation of $SmNiO_3/LaAlO_3$. Nevertheless, in these cases, a single crystalline epitaxial layer of $RENiO_3$ is observed adjacent to the surface of

the substrate with a thickness of ~10 nm, as its composition is confirmed by the respective energy dispersive spectrometer (EDS) mappings as shown in Fig. S4. By further increasing the film thickness, the same crystal orientation compared to the $LaAlO_3$ substrate cannot be preserved and polycrystalline $RENiO_3$ is observed. The polycrystallinity of $RENiO_3$ adjacent to the surface is further supported by the X-ray grazing incident diffraction pattern as shown in Fig. S5.

It is also worth noticing that the $RENiO_3$ thin films used by the present MOD approach, such as $NdNiO_3$ and $SmNiO_3$, can be also successfully grown on quartz, in which situation there is no epitaxy relationship between the film and substrate. Fig. S6 shows the representative cross-section morphologies of the $NdNiO_3$ film grown on quartz substrate, in which case the thin film is in polycrystallinity. Fig. S7 further demonstrates the respective diffraction pattern, as obtained by accumulating the transmission electronic microscopic figures shown in Fig. S6, where the diffraction rings associated to the perovskite structure are clearly demonstrated.

3.2. Temperature induced MIT properties

To characterize the critical temperature (T_{MIT}) induced metal to insulator transitions properties of the $RENiO_3$/$LaAlO_3$ (001) samples grown by using the MOD, their resistivity dependent on temperature (ρ–T) are compared in Fig. 2(a). The expected metal to insulator transitions at T_{MIT} are clearly observed for as-grown $NdNiO_3$, $Sm_xNd_{1-x}NiO_3$, $SmNiO_3$, $EuNiO_3$, and $GdNiO_3$ samples. Fig. 2(b) further shows the magnitude of T_{MIT} that reaches the general agreement compared to the previous reports [14–15,33–34]. Also similar to the previous investigations [35], the T_{MIT} cannot be electrically measured for $RENiO_3$ thin film samples at high metastability (e.g. $DyNiO_3$, $YNiO_3$, $HoNiO_3$, $TbNiO_3$ and $ErNiO_3$). Nevertheless, the formation of their electronic phases in metastable manner is indicated by the reducing ρ–T

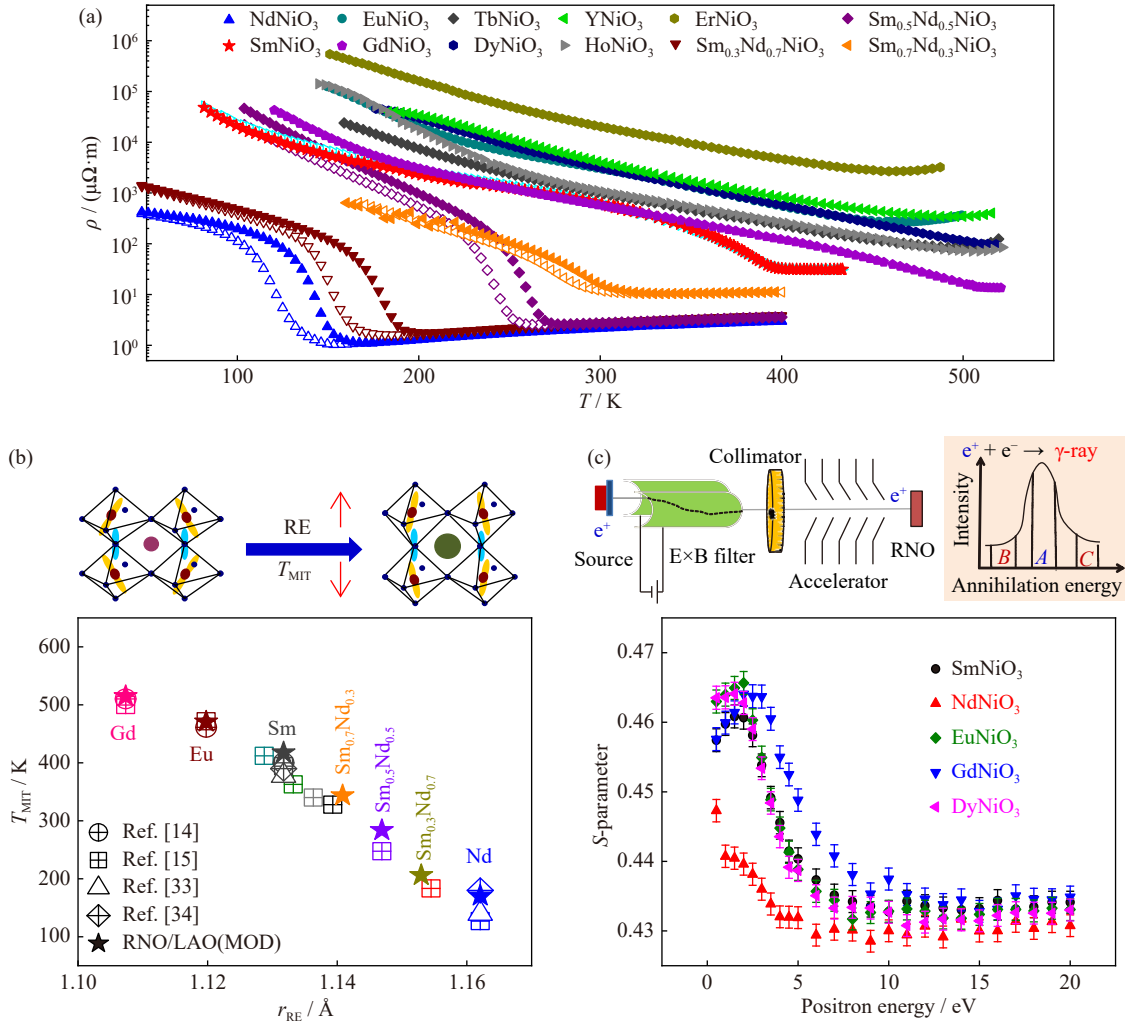

Fig. 2. (a) Temperature dependence of the resistivity measured for the $RENiO_3/LaAlO_3$ (001) grown by the high oxygen pressure assisted metal-organic deposition (MOD) approach. (b) As achieved metal to insulator transition temperature (T_{MIT}) compared to the previous reports in Refs. [14–15,33–34]. The above sketch illustrates the released distortion in the NiO_6 octahedron with an increasing ionic radius of RE (r_{RE}) that reduces T_{MIT}. (c) The S-parameter of the $RENiO_3$ (RNO) grown by MOD measured by the positron annihilation spectroscopy (PAS). As the working principle of PAS illustrated by the above sketch, the S-parameter is derived from the shape of the Doppler broadening spectroscopy (DBS) of the annihilation generated γ-ray by $A/(A + B + C)$. The E×B Filter is the positron energy filter with orthogonal electric and magnetic fields.

tendencies observed in their insulating phases, which is in agreement to the expected negative temperature dependence thermistor transportation [15,35]. It is also worth noticing that the MIT behavior can be also achieved in the non-epitaxially grown $RENiO_3$/quartz with light or middle rare-earth compositions, as a representative case demonstrated in Fig. S8 for as-grown $SmNiO_3$/quartz. It can be seen that as grown film exhibits perovskite structure in polycrystallinity, while the MIT property was also electronically detectable. Therefore, a heterogeneous nucleation process via coherency with the template of the substrate is not necessary for the MOD growth of $RENiO_3$ thin film in this work.

3.3. Lattice defects probed by PAS

To further probe the defects within the $RENiO_3/LaAlO_3$ grown by MOD, the positron annihilation spectroscopy (PAS) measurements were further performed based on ^{22}Na source that generates positron beams with continuously adjustable incident energy (E_K) [21,36]. The defect amount within $RENiO_3$ is indicated by their DBS from their positron annihilation induced γ-ray profile, as detected at various E_K that reflects the positron penetration depth (t_P) following $t_P = (40D^{-1})\ E_K^{1.6}$, where D represents the material density. Positron annihilation with the localized low momentum electrons at defect regions elevates the *S*-parameters derived from the DBS, while annihilation with inner shell electrons associated to the material lattice contributes to the complementary *W*-parameters. Fig. 2(c) shows the *S*-parameter of as-grown $RENiO_3/LaAlO_3$ with various rare-earth elements, while their respective *W*-parameters and the *W*–*S* relationship are demonstrated in Fig. S9. In general, enlarging the size of RE results in the reduction in the *S*-parameter (see Fig. 2(c)) and elevate the *W*-parameters (see Fig. S9), and this indicates the reduction of lattice defects in as-grown $RENiO_3$ thin films with larger rare-earth element. It is also worth noticing that the presently grown $SmNiO_3$ thin films exhibit larger *S*-parameters as compared to the respective single crystalline samples reported in Ref. [19], and this demonstrates the elevation in their lattice defects. The increased lattice defect within $RENiO_3$ with heavier rare-earth composition should be attributed to their more distorted NiO_6 octahedron and lower material stability, and therefore more lattice defect is expected.

3.4. Hydrogen induced electronic transition properties

In contrast to the timely heterogenous crystallization of the arriving percussors in the epitaxial growth of $RENiO_3$ using vacuum-based physical vapor depositions (e.g. PLD), the isooctanoate based chemical precursors of RE and Ni were stacked on the surface of the substrate at a relatively large thickness (e.g. ~100 nm). In that case, the afterward crystallization of the precursors via high pressure annealing is much less controllable compared to the PLD process. For the case MOD growth for $SmNiO_3$, the chemical precursors located adjacent to the substrate crystallized via heterogenous nucleation along the crystal orientation of the $LaAlO_3$ substrate to form a quasi-single crystalline layer, while at the same time a homogeneous nucleation is expected for the precursors away from the interface that grows as the polycrystalline layer. Although the $NdNiO_3$ grown by MOD exhibits smaller positive formation free energy that may count for its better preservation of an epitaxy relationship to the substrate, it is expected to be more defective (e.g. with more anti-site defects) compared to the ones grown via vacuum depositions.

The variation in the state of lattice defects is expected to influence the hydrogen diffusion kinetics within $RENiO_3$ that triggers the Mottronic orbital transitions among $t_{2g}^6e_g^1$ (or $t_{2g}^6e_g^{1\pm\delta}$), $t_{2g}^6e_g^2$, and $t_{2g}^6e_g^3$ to regulate the material resistivity [21]. In Fig. 3(a), the initial resistance (R_0) and hydrogenation resistance (R_H) of the $RENiO_3$ grown by MOD (with top platinum catalyst electrode, as illustrated in Fig. S10) are compared for various rare-earth compositions. Figs. S11–S24 show the characteristic current–voltage (*I*–*V*) curve as measured for the $RENiO_3$ samples before and after the hydrogenation process. It can be seen that the *I*–*V* characterizations were all with Ohm content, while the hydrogenation increases the resistance for most samples. In general, a reducing tendency is observed in the resistance of the pristine $RENiO_3$ before hydrogenation when enlarging RE, while the hydrogenation process effectively increases the material resistance of $RENiO_3$ by several orders of magnitudes. As the relative elevation in their resistances upon hydrogenation (R_H/R_0) more clearly compared in Fig. 3(b), it is interesting to note that the R_H/R_0 shows a non-monotonic tendency with the size of RE, and the maximum in R_H/R_0 is observed for $NdNiO_3$. It is also worth noticing that the R_H/R_0 of the presently grown $NdNiO_3$, $SmNiO_3$, $Sm_xNd_{1-x}NiO_3$, and $EuNiO_3$ by MOD largely exceed the ones observed for their single crystalline counterparts. As a typical case, the R_H/R_0 for the $NdNiO_3$ grown by MOD exceeds 10^9, the magnitude of which is 6 orders larger than the one achieved in single crystalline $NdNiO_3$ grown by spin coating [37].

The above observed non-monotonic tendency in the electronic transition as triggered by hydrogen differs to the previous expectation that the resistance of $RENiO_3$ with smaller RE should be more increased upon the same hydrogenation process [38]. It is also worth noticing that the expected increasing tendency in R_H/R_0 with the reducing size of RE is indeed observed for quasi-single crystalline $RENiO_3$ thin films grown by using the previously reported spin coating approach based on $RE(NO_3)_3$ and $Ni(AC)_2$ precursors [15]. This reveals the dominate role associated to the lattice defects in the regulating the quantum transition properties of $RENiO_3$ upon hydrogenations, in addition to the rare-earth composition as known to determine their intrinsic electronic orbital configurations [14]. The hydrogenated $RENiO_3$ exhibits highly insulating transportation behavior, as one representative temperature dependence of resistance shown in Fig. S25 for $SmNiO_3/LaAlO_3$ upon hydrogenation. Apart from annealing in hydrogen, a more pronounced variation in resistivity is also observed for the $RENiO_3$ grown via MOD when triggering the electronic transition electrochemically (see Fig. S26).

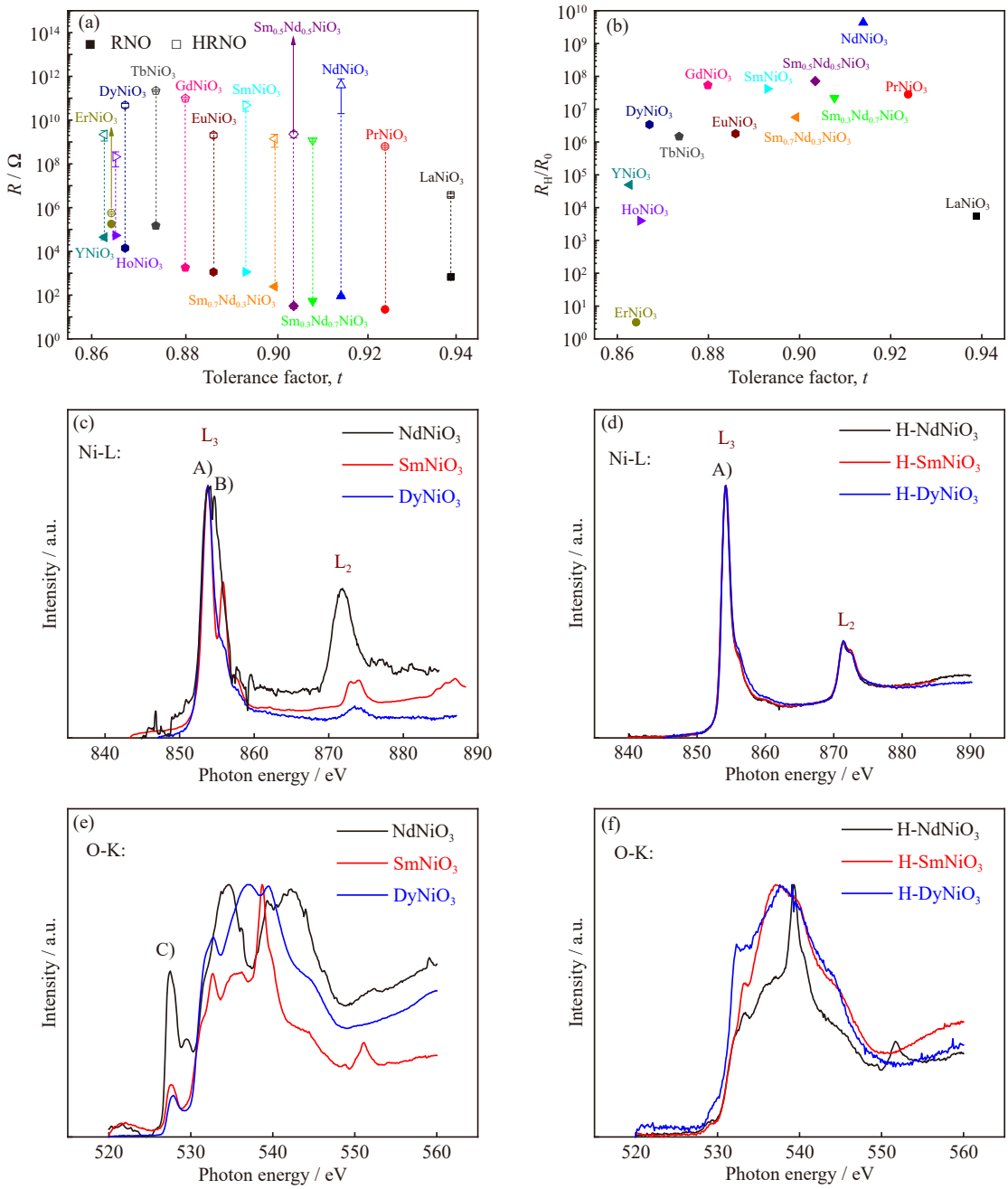

Fig. 3. (a) The resistance of the platinum patterned $RENiO_3/LaAlO_3$ (001) grown by the high oxygen pressure assisted metal-organic deposition (MOD) approach before (solid square for RNO) and after (hollow square for H-$RENiO_3$ (HRNO)) the hydrogenation process. (b) The elevation in the resistance of $RENiO_3/LaAlO_3$ (001) upon hydrogenation (solid symbols), as compared to the ones obtained from Ref. [34] (hollow symbols). (c–f) The near edge X-ray absorption fine structure (NEXAFS) analysis of as-grown $RENiO_3/LaAlO_3$ (001): the Ni-L edge (c) prior to and (d) after the hydrogenation; the O-K edge (e) prior to and (f) after the hydrogenation.

3.5. Electronic structures probed by NEXAFS

As demonstrated in Fig. 3(c–d), the Ni-L_3 spectrum (reflecting Ni-2p→Ni-3d transition) of $RENiO_3$ is split into two peaks that associated to $t_{2g}^6e_g^2(Ni^{2+}$, Peak A) and $t_{2g}^6e_g^1(Ni^{3+}$, Peak B), respectively [15–16,39–41]. For pristine samples in Fig. 3(c), a lower intensity in Peak B compared to A is observed for $RENiO_3$ with a reducing size of RE, indicating the elevation in the insulating orbital configurations compared to the metallic ones [16,39–40]. This observation is in agreement to the enhancement in T_{MIT} when reducing the size of rare-earth element in $RENiO_3$ as known previously [15]. The hydrogenation process nearly eliminates the Peak B in the Ni-L_3 spectrum, and results in overlapped Ni-L_3 and Ni-L_2 spectrums for all hydrogenated $RENiO_3$ with various rare-earth compositions. This is a strong indication of the orbital transitions of $RENiO_3$ from the electron itinerant $t_{2g}^6e_g^{1\pm\delta}$ (or $t_{2g}^6e_g^1$) towards the electron localized $t_{2g}^6e_g^2$ orbital configurations as triggered by the hydrogenation process [16].

Further consistency is observed in the variation of the

NEXAFS of O-K, as the results demonstrated in Fig. 3(e) and (f) for the same $RENiO_3$ samples before and after hydrogenation, respectively. For example, the pre-peak (of –529 eV) in the O-K spectrum originating from Ni: 3d–O: 2p hybridization shows a reducing tendency for pristine $RENiO_3$ with a reducing size of RE in Fig. 3(e). It indicates the elevation in the formation of oxygen vacancy in $RENiO_3$ with smaller RE elements, and is in agreement to the previous reports [16,41]. From the following hydrogenation process, the O-K pre-peaks are nearly erased for all hydrogenated $RENiO_3$ samples in Fig. 3(f), indicating the orbital transitions from $t_{2g}^6 e_g^{1\pm\delta}$ (or $t_{2g}^6 e_g^1$) to $t_{2g}^6 e_g^2$ upon hydrogenation. In addition, it is more interesting to note the reducing tendency in the relative distribution of O-K edge of the hydrogenated $RENiO_3$ at lower photon energies (e.g. 532–538 eV) with an enlarging size of RE.

3.6. Hydrogen composition probed by NRA

As illustrated in Fig. 4(a), the NRA utilizes the nuclear resonance between the incident $^{15}N^{2+}$ ions from accelerator with the ^1H within the material at a characteristic incident kinetic energy at 6.385 MeV that emits detectable gamma-rays [42–44]. To establish the depth profile of ^1H within $RENiO_3$, the incident kinetic energy of $^{15}N^{2+}$ is gradually enlarged from 6.385 eV, in which situation the resonance depth is increased by an energy cross section of 3.195 keV/nm times the penetration depth. Fig. 4(b–c) and Fig. S27 show representative NRA spectrums for the $NdNiO_3/LaAlO_3$, $SmNiO_3/LaAlO_3$, $GdNiO_3/LaAlO_3$, and $DyNiO_3/LaAlO_3$ as grown by MOD before and after the hydrogenation process. Prior to the hydrogenation process, a lower hydrogen concentration base signal from water absorption is observed for $NdNiO_3$ (e.g. $\sim 4 \times 10^{20}$ cm^{-3}) compared to $SmNiO_3$, $GdNiO_3$, and $DyNiO_3$ (e.g. $1.5 \times 10^{21} - 2.3 \times 10^{21}$ cm^{-3}). This observation is in agreement to the PAS results as shown in Fig. 2(c) that as-grown $NdNiO_3/LaAlO_3$ exhibits the lowest defect concentration and therefore the water absorption concentration is also the lowest. By further annealing in hydrogen at the same condition, the hydrogen concentrations associated to the thin film materials increase for all the $RENiO_3/LaAlO_3$ samples, and this is a strong indication of the hydrogen incorporation within $RENiO_3$. It is worth noticing that the dangling bonds associated with the lattice defect within the chemically grown $RENiO_3$ thin films are easily passivated by the hydrogen during annealing, and this will enhance the hydrogen incorporation concentration.

In Fig. 4(d), the depth distribution of the net concentration of hydrogen incorporation is further calculated by the subtracting the NRA spectrum for the pristine $RENiO_3$ from the one for the hydrogenated samples. In general, the net incorporation concentrations of hydrogen within $RENiO_3$ samples are of 2×10^{21}–3×10^{21} cm^{-3}, a magnitude of which can sufficiently trigger the orbital transition from electron itinerant Ni^{3+} $t_{2g}^6 e_g^1$ state to the electron localized Ni^{2+} $t_{2g}^6 e_g^2$ state. Nevertheless, this is not expected to arouse further electronic transitions towards Ni^{1+} $t_{2g}^6 e_g^3$ that requires a hydrogen concentration at least beyond 4×10^{21} cm^{-3} [21]. In Fig. 4(e), the magnitude of R_H/R_0 is plotted as a function of the hydrogen concentration for $SmNiO_3$ and $NdNiO_3$ samples grown in this work and also from the previous reports [21,43]. In general, an increasing tendency in R_H/R_0 is observed for both $SmNiO_3$ and $NdNiO_3$ with an increasing concentration in the hydrogen incorporation, and this is in consistency to our understanding that the elevation in their resistivity is associated with the Ni^{3+} $t_{2g}^6 e_g^1$ to Ni^{2+} $t_{2g}^6 e_g^2$ orbital transition.

From the above results, it can be seen that more pronounced variations in the resistivity as well as the electronic structures upon hydrogenation are observed for $RENiO_3$ at lower metastability as presently grown via MOD. This tendency is in contrast to the previously reports that larger variation in resistivity was observed for $RENiO_3$ at higher metastability as grown by using vacuum based approaches [38]. Noticing the higher defect concentrations as observed for the chemically grown $RENiO_3$ samples compared to the vacuum deposited ones at similar thickness, it reveals the extrinsic regulations in their hydrogen induced electronic transition properties associated to the lattice defects.

Fig. 4(f) illustrated the NiO_6 octahedron (according to Ref. [10]) and also their respective band structure (according to Ref. [4]) for $RENiO_3$ at semiconductive phase, metallic phase, defective metallic phase, and the hydrogenated insulating phase. The charge (or electron) transfer between the hydrogen and the d-band of Ni is expected to be intrinsically relevant to the bending in the Ni–O–Ni bond angle. As illustrated by the left two figures in Fig. 4(f), the Ni–O–Ni bond angle for the Ni^{3+} based semiconductive $RENiO_3$ ($t_{2g}^6 e_g^{1\pm\delta}$) with heavier rare-earth compositions exceeds the one for the metallic $RENiO_3$ ($t_{2g}^6 e_g^1$) with lighter rare-earth compositions, and this results in more effective electron transfer from the incorporated hydrogen to the lattice Ni owing to its larger polarity in Ni–O–Ni bond. This understanding is supported by the previous observation that the semiconductive $RENiO_3$ (with smaller ionic radius of RE) experienced larger elevation in their material resistivity upon hydrogenation, compared to the metallic one [32–33]. Nevertheless, the above electron transfer from hydrogen to metallic $RENiO_3$ can be extrinsically improved by introducing the lattice defects, in which situation the passivation of the dangling bonds enhances the hydrogen incorporation amount to more effectively reduce Ni^{3+} to Ni^{2+}, as illustrated by the second figure in Fig. 4(f) from the right. This is clearly demonstrated by the higher hydrogen incorporation composition as observed in the presently grown $RENiO_3$ thin films via MOD compared to the ones grown by PLD, as summarized in Fig. 4(e). It is also worth noticing that the $RENiO_3$ thin films with various rare-earth compositions reached a similar electronic ground state relevant to Ni^{2+} ground state after the hydrogenation process, as is indicated by their similar NEXAFS spectrum shown in Fig. 3(d). Therefore, although the rare-earth composition significantly influences the electronic structure associated with Ni^{3+} (or $Ni^{3+\delta}$) and also their metal to insulator transition properties, these $RENiO_3$ is likely to transit to-

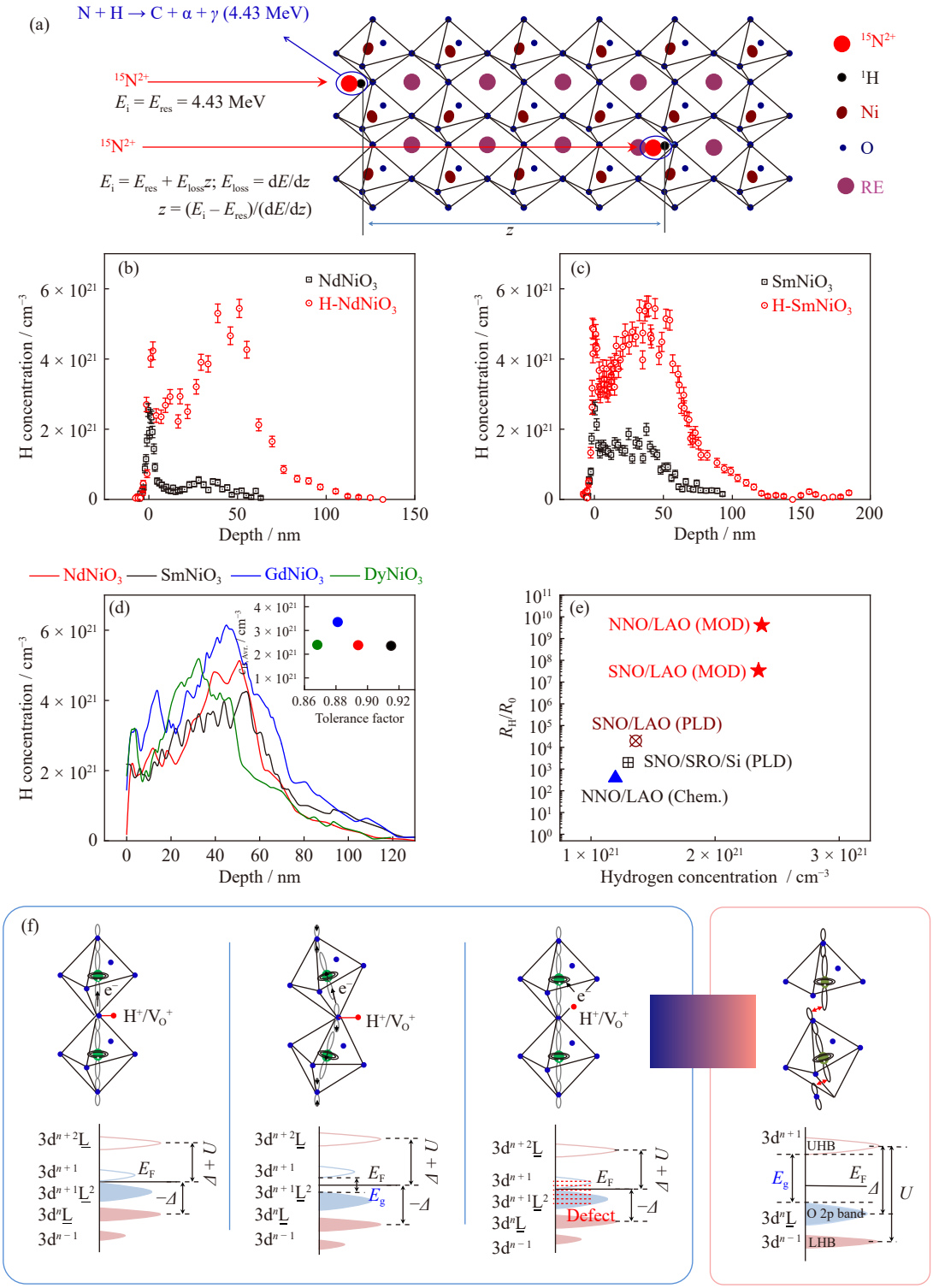

Fig. 4. **(a) The working principle of the resonant nuclear reaction analysis (NRA) that achieves the quantitative detection of the depth profile of hydrogen (^{1}H or ^{1}H$^+$) within $RENiO_3$. E_i is the incident kinetic energy of $^{15}N^{2+}$. E_{res} and E_{loss} are the resonance energy and loss energy in a nuclear reaction, respectively. z is the ion trajectory length below the target surface. The depth profile of the hydrogen concentration ($C_{H,Avr}$) within as-grown $NdNiO_3$ (b) and $SmNiO_3$ (c) as measured before and after the hydrogenation process via NRA, while the ones for $GdNiO_3$ and $DyNiO_3$ are demonstrated in Fig. S27. (d) Net incorporation in the hydrogen concentration within $RENiO_3$ with various rare-earth compositions during their hydrogen triggered electronic transitions. (e) The elevation in the resistivity of $RENiO_3$ induced by hydrogenation plotted as a function of the incorporated hydrogen concentration as compared for the present samples grown by the high oxygen pressure assisted metal-organic deposition as well as the previous reports [21,43]. SRO/Si is the $SrRuO_3$ thin film deposited on Si substrate. (f) Schematic illustration of the charge and orbital transfer during the hydrogen induced electronic transitions for the metallic phase, insulating phase, and defect enriched metallic phase of $RENiO_3$. E_F is the Fermi energy level. E_g is the energy band gap. U represents the Coulomb interaction between electrons, and Δ is the charge transfer energy. UHB and LHB are the upper and lower Hubbard Band, respectively.**

wards a similar ground electronic state associated with Ni^{2+} upon hydrogenation.

From the perspective of orbital transition, $RENiO_3$ at lower metastability (e.g. $NdNiO_3$) should experience more significant variations in their electronic structure during the orbital transition from the metallic $t_{2g}^6e_g^1$ to highly insulating $t_{2g}^6e_g^2$, compared to the one from semiconductive $t_{2g}^6e_g^{1\pm\delta}$. Nevertheless, such transition is impeded kinetically owing to the ineffective electron transfer from the hydrogen dopant to the lattice of metallic $RENiO_3$ at low hydrogenation temperatures or small electrochemistry electric fields, owing to the lower polarity in their less bended Ni–O–Ni bonds by enlarging the rare-earth ionic radius [14]. This well explains the smaller elevation in resistivity of the previous quasi-single crystalline $NdNiO_3$ upon hydrogenation, noticing the larger ionic radius of Nd compared to Sm or Eu[32].

Extrinsically introducing lattice defects within $RENiO_3$ (e.g. grown by MOD) is expected to promote the electron transfer from hydrogen dopant to the material lattice via the passivation process that reduces the energy barrier to trigger the orbital transitions [21]. It is in particular worthy to note that this extrinsic impact associated to lattice defect plays a dominate role for $RENiO_3$ in metallic phase or at low metastability that explains the more significant enhancement in R_H/R_0 for the MOD grown $NdNiO_3$ by 9 orders. In contrast, the hydrogen induced electronic transition of $RENiO_3$ at high metastability is expected to be more dominated by the intrinsic distortion of the NiO_6 octahedron and more easily saturated by reaching the $t_{2g}^6e_g^2$ terminal electronic state. This understanding is in well agreement in the observed reducing tendency in R_H/R_0 by further elevating the atomic weight of RE of $RENiO_3$ beyond Sm, despite the similar hydrogen incorporation concentration as quantified by NRA as shown in Fig. 4(d).

4. Conclusions

In conclusion, a vacuum free metal-organic decomposition approach was developed to grow $RENiO_3$ thin films that combines the high adjustability in the rare-earth compositions associated with the wet chemical growth and a comparable large deposition thickness to the vacuum depositions (e.g. ~100 nm). The high chemical reactivity of the isooctanoate based metal organic precursors kinetically promotes the formation of $RENiO_3$ as metastable perovskites and relives their reliance to the heterogeneous growth via interfacial coherence. As a result, the growths of $RENiO_3$ are tolerant to the lattice defects or misfits to achieve larger deposition thickness or even in polycrystallinity, as indicated by PAS. The defect enriched $RENiO_3$ as grown by MOD improves the hydrogen incorporation composition up to 2×10^{21} cm^{-3} and also their electron transfer with the NiO_6 octahedron, resulting in more significant variations in their electronic structures and transportation properties. It is expected that such defect engineering provides an extrinsic strategy to regulate the hydrogen induced quantum transitions of $RENiO_3$ via the kinetic electron acceptance from hydrogen, apart from the intrinsic adjustment in the orbital configurations via the rare-earth composition. This paves the way to improve the performance of correlated electronic devices utilizing the hydrogen induced quantum transitions of $RENiO_3$, e.g. ocean electric field sensor, bio-sensor, and neuron synapse logical devices.

Acknowledgements

This work was financially supported by the National Key Research and Development Program of China (No. 2021YFA0718900) and National Natural Science Foundation of China (Nos. 62074014, 52073090, and 52103284). Prof. Jikun Chen also acknowledges Xiaomi Scholar. The authors appreciate helpful discussions and technical supports by Profs. Markus Wilde, Katsuyuki Fukutani, Bunshi Fugetsu, and Ichiro Sakata from The University of Tokyo (Japan). In addition, we also acknowledge Dr. Chen Liu from Institute of High Energy Physics, Chinese Academy of Sciences for providing technical support in the synchrotron-based analysis (4B9B photoemission station).

Conflict of Interest

Jikun Chen is a youth editorial board member for this journal and not involved in the editorial review or the decision to publish this article. The authors declare that they have no conflict of interest.

Supplementary Information

The online version contains supplementary material at https://doi.org/10.1007/s12613-023-2703-9.

References

[1] Z. Zhang, D. Schwanz, B. Narayanan, *et al*., Perovskite nickelates as electric-field sensors in salt water, *Nature*, 553(2018), No. 7686, p. 68.

[2] Y. Zhou, X.F. Guan, H. Zhou, *et al*., Strongly correlated perovskite fuel cells, *Nature*, 534(2016), No. 7606, p. 231.

[3] Y.F. Sun, M. Kotiuga, D. Lim, *et al*., Strongly correlated perovskite lithium ion shuttles, *Proc. Natl. Acad. Sci. USA*, 115(2018), No. 39, p. 9672.

[4] J. Shi, Y. Zhou, and S. Ramanathan, Colossal resistance switching and band gap modulation in a perovskite nickelate by electron doping, *Nat. Commun.*, 5(2014), art. No. 4860.

[5] F. Zuo, P. Panda, M. Kotiuga, *et al*., Habituation based synaptic plasticity and organismic learning in a quantum perovskite, *Nat. Commun.*, 8(2017), No. 1, art. No. 240.

[6] H.T. Zhang, T.J. Park, I.A. Zaluzhnyy, *et al*., Perovskite neural trees, *Nat. Commun.*, 11(2020), No. 1, art. No. 2245.

[7] H.T. Zhang, F. Zuo, F. Li, *et al*., Perovskite nickelates as bio-electronic interfaces, *Nat. Commun.*, 10(2019), No. 1, art. No. 1651.

[8] H. Yoon, M. Choi, T.W. Lim, *et al*., Reversible phase modulation and hydrogen storage in multivalent VO_2 epitaxial thin films, *Nat. Mater.*, 15(2016), No. 10, p. 1113.

[9] N.P. Lu, P.F. Zhang, Q.H. Zhang, *et al*., Electric-field control of

tri-state phase transformation with a selective dual-ion switch, *Nature*, 546(2017), No. 7656, p. 124.
[10] Z.X. Wei, Z.Y. Wang, C.Q. Xu, *et al*., Defect-induced insulator-metal transition and negative permittivity in $La_{1-x}Ba_xCoO_3$ perovskite structure, *J. Mater. Sci. Technol.*, 112(2022), p. 77.
[11] S.J. Fang, Z.Y. Pang, F.G. Wang, L. Lin, and S.H. Han, Annealing effect on transport and magnetic properties of $La_{0.67}Sr_{0.33}MnO_3$ thin films grown on glass substrates by RF magnetron sputtering, *J. Mater. Sci. Technol.*, 27(2011), No. 3, p. 223.
[12] X.F. Zhou, Z.R. Jia, A.L. Feng, *et al*., Synthesis of fish skin-derived 3D carbon foams with broadened bandwidth and excellent electromagnetic wave absorption performance, *Carbon*, 152(2019), p. 827.
[13] H.J. Wu, G.L. Wu, and L.D. Wang, Peculiar porous α-Fe_2O_3, γ-Fe_2O_3 and Fe_3O_4 nanospheres: Facile synthesis and electromagnetic properties, *Powder Technol.*, 269(2015), p. 443.
[14] G. Catalan, Progress in perovskite nickelate research, *Phase Transitions*, 81(2008), No. 7-8, p. 729.
[15] J.K. Chen, H.Y. Hu, J.O. Wang, *et al*., Overcoming synthetic metastabilities and revealing metal-to-insulator transition & thermistor bi-functionalities for d-band correlation perovskite nickelates, *Mater. Horiz.*, 6(2019), No. 4, p. 788.
[16] J.R. Li, R.J. Green, Z. Zhang, *et al*., Sudden collapse of magnetic order in oxygen-deficient nickelate films, *Phys. Rev. Lett.*, 126(2021), No. 18, art. No. 187602.
[17] R. Jaramillo, S.D. Ha, D.M. Silevitch, and S. Ramanathan, Origins of bad-metal conductivity and the insulator-metal transition in the rare-earth nickelates, *Nat. Phys.*, 10(2014), No. 4, p. 304.
[18] J.S. Zhou, J.B. Goodenough, and B. Dabrowski, Pressure-induced non-fermi-liquid behavior of $PrNiO_3$, *Phys. Rev. Lett.*, 94(2005), No. 22, art. No. 226602.
[19] I.I. Mazin, D.I. Khomskii, R. Lengsdorf, *et al*., Charge ordering as alternative to Jahn–Teller distortion, *Phys. Rev. Lett.*, 98(2007), No. 17, art. No. 176406.
[20] D. Li, K. Lee, B.Y. Wang, *et al*., Superconductivity in an infinite-layer nickelate, *Nature*, 572(2019), No. 7771, p. 624.
[21] J.K. Chen, W. Mao, L. Gao, *et al*., Electron-doping mottronics in strongly correlated perovskite, *Adv. Mater.*, 32(2020), No. 6, art. No. 1905060.
[22] H. Lu, M. Rossi, A. Nag, *et al*., Magnetic excitations in infinite-layer nickelates, *Science*, 373(2021), No. 6551, p. 213.
[23] E. Been, W.S. Lee, H.Y. Hwang, *et al*., Electronic structure trends across the rare-earth series in superconducting infinite-layer nickelates, *Phys. Rev. X*, 11(2021), No. 1, art. No. 011050.
[24] H.F. Li, F.Q. Meng, Y. Bian, *et al*., Frequency regulation in alternation-current transports across metal to insulator transitions of thin film correlated perovskite nickelates, *J. Mater. Sci. Technol.*, 148(2023), p. 235.
[25] R. Jaramillo, F. Schoofs, S.D. Ha and S. Ramanathan, High pressure synthesis of $SmNiO_3$ thin films and implications for thermodynamics of the nickelates, *J. Mater. Chem. C*, 1(2013), No. 13, p. 2455.
[26] N. Shukla, T. Joshi, S. Dasgupta, P. Borisov, D. Lederman, and S. Datta, Electrically induced insulator to metal transition in epitaxial $SmNiO_3$ thin films, *Appl. Phys. Lett.*, 105(2014), No. 1, art. No. 012108.
[27] A. Ambrosini and J.F. Hamet, Sm_xNd_{1-x} NiO_3 thin-film solid solutions with tunable metal–insulator transition synthesized by alternate-target pulsed-laser deposition, *Appl. Phys. Lett.*, 82(2003), No. 5, p. 727.
[28] J. Shi, S.D. Ha, Y. Zhou, F. Schoofs, and S. Ramanathan, A correlated nickelate synaptic transistor, *Nat. Commun.*, 4(2013), art. No. 2676.
[29] F.Y. Bruno, K.Z. Rushchanskii, S. Valencia, *et al*., Rationalizing strain engineering effects in rare-earth nickelates, *Phys. Rev. B*, 88(2013), No. 19, art. No. 195108.
[30] F. Conchon, A. Boulle, R. Guinebretière, *et al*., Effect of tensile and compressive strains on the transport properties of $SmNiO_3$ layers epitaxially grown on (001) $SrTiO_3$ and $LaAlO_3$ substrates, *Appl. Phys. Lett.*, 91(2007), No. 19, art. No. 192110.
[31] R.W. Vest, Metallo-organic decomposition (MOD) processing of ferroelectric and electro-optic films: A review, *Ferroelectrics*, 102(1990), No. 1, p. 53.
[32] G.M. Vest and S. Singaram, Synthesis of metallo-organic compounds for mod powders and films, *MRS Online Proc. Libr.*, 60(1985), No. 1, p. 35.
[33] I.V. Nikulin, M.A. Novojilov, A.R. Kaul, S.N. Mudretsova, and S.V. Kondrashov, Oxygen nonstoichiometry of $NdNiO_{3-\delta}$ and $SmNiO_{3-\delta}$, *Mater. Res. Bull.*, 39(2004), No. 6, p. 775.
[34] M.T. Escote, A.M.L. da Silva, J.R. Matos, and R.F. Jardim, General properties of polycrystalline $LnNiO_3$ (Ln = Pr, Nd, Sm) compounds prepared through different precursors, *J. Solid State Chem.*, 151(2000), No. 2, p. 298.
[35] J.K. Chen, H.Y. Hu, J.O. Wang, *et al*., A d-band electron correlated thermoelectric thermistor established in metastable perovskite family of rare-earth nickelates, *ACS Appl. Mater. Interfaces*, 11(2019), No. 37, p. 34128.
[36] B.Y. Wang, Y.Y. Ma, Z. Zhang, R.S. Yu, and P. Wang, Performance of the Beijing pulsed variable-energy positron beam, *Appl. Surf. Sci.*, 255(2008), No. 1, p. 119.
[37] Y. Bian, H.Y. Li, F.B. Yan, *et al*., Hydrogen induced electronic transition within correlated perovskite nickelates with heavy rare-earth composition, *Appl. Phys. Lett.*, 120(2022), No. 9, art. No. 092103.
[38] J.K. Chen, Y. Zhou, S. Middey, *et al*., Self-limited kinetics of electron doping in correlated oxides, *Appl. Phys. Lett.*, 107(2015), No. 3, art. No. 031905.
[39] K. Kleiner, J. Melke, M. Merz, *et al*., Unraveling the degradation process of $LiNi_{0.8}Co_{0.15}Al_{0.05}O_2$ electrodes in commercial lithium ion batteries by electronic structure investigations, *ACS Appl. Mater. Interfaces*, 7(2015), No. 35, p. 19589.
[40] L.A. Montoro, M. Abbate, and J.M. Rosolen, Electronic structure of transition metal ions in deintercalated and reintercalated $LiCo_{0.5}Ni_{0.5}O_2$, *J. Electrochem. Soc.*, 147(2000), No. 5, art. No. 1651.
[41] H. Kobayashi, M. Shikano, S. Koike, H. Sakaebe, and K. Tatsumi, Investigation of positive electrodes after cycle testing of high-power Li-ion battery cells, *J. Power Sources*, 174(2007), No. 2, p. 380.
[42] M. Wilde and K. Fukutani, Hydrogen detection near surfaces and shallow interfaces with resonant nuclear reaction analysis, *Surf. Sci. Rep.*, 69(2014), No. 4, p. 196.
[43] J.K. Chen, W. Mao, B.H. Ge, *et al*., Revealing the role of lattice distortions in the hydrogen-induced metal-insulator transition of $SmNiO_3$, *Nat. Commun.*, 10(2019), No. 1, art. No. 694.
[44] W. Mao, M. Wilde, T. Chikada, *et al*., Fabrication and hydrogen permeation properties of epitaxial Er_2O_3 films revealed by nuclear reaction analysis, *J. Phys. Chem. C*, 120(2016), No. 28, p. 15147.